Droplet detachment from a vertical filament with one end clamped

Droplet detachment from a vertical filament with one end clamped

Meng Lu,[1] Xuerui Mao,[2] Luca Brandt,[3] and Jian Deng[1,*]

[1]*State Key Laboratory of Fluid Power and Mechatronic Systems, Department of Mechanics, Zhejiang University, Hangzhou 310027, People's Republic of China*

[2]*Advanced Research Institute of Multidisciplinary Sciences, Beijing Institute of Technology, Beijing 100081, People's Republic of China*

[3]*Department of Environmental, Land and Infrastructure Engineering, Politecnico di Torino, 10129 Turin, Italy*

(Received 7 April 2024; accepted 12 September 2024; published 2 October 2024)

Understanding whether a droplet adheres to or detaches from a flexible filament upon axial impact is of significant interest, particularly in the context of raindrop impact on natural surfaces. This process involves dynamic buckling followed by mode coarsening, dissipating the initial droplet kinetic energy and converting the remaining into elastic energy of the filament. To elucidate this phenomenon, we construct two phase diagrams, one while fixing the filament height and the other the droplet diameter. Notably, we observe that the energy conversion rate is inversely proportional to a Cauchy number, defining the transition between attached and detached droplet in the filament length–falling height diagram. This enables us to derive an expression for the critical falling height as a function of the filament parameters, accounting for the energy conversion rate, which emerges as a key factor for droplet detachment.

DOI: 10.1103/PhysRevResearch.6.043003

I. INTRODUCTION

Exposure to raindrops is critical for natural species, influencing various ecological and physiological aspects. For example, the impact of rain on plants can initiate numerous processes, including the dispersal of pathogens and propagules, the erosion of leaf wax, and gas exchange [1,2]. Prolonged wetness on leaves during rainfall can impede key physiological processes like transpiration and photosynthesis, potentially leading to reduced plant growth and vigor [3]. To mitigate this, plants have evolved mechanisms such as leaf vibration to dislodge water droplets, thereby minimizing the adverse effects of sustained wetness. Grass and delicate leaves, akin to membranes and filaments, exhibit significant deflection to facilitate the sliding of droplets to the ground, thereby enhancing water uptake by root systems [4].

Similarly, animals utilize epicuticular hairy structures to actively shed water droplets, reducing the risk of hypothermia [5] and minimizing energy expenditure associated with water carriage and evaporation [6]. Inspired by various biological features, such as dandelion pappi [7], legs of water striders [8], cactus spines [9], and spider silk [10], researchers have developed biofibers capable of directionally steering and transporting droplets [11,12]. These biomimetic advancements have practical applications, such as artificial fog harvesters designed to efficiently collect water from the air. These devices leverage principles observed in natural systems to optimize water collection, particularly in arid regions where water scarcity is a significant concern [13–15]. Therefore, understanding whether droplets adhere to or rebound off structures after impact is critical.

The impact of droplets on rigid substrates or elastomers has been extensively studied over decades. Researchers primarily focus on the morphology and motion of the droplet, with particular attention paid to the wetting properties and flexibility of the substrate [16–18]. For example, on hydrophobic surfaces, the droplets are more likely to bounce back [19–21], while droplets on soft substrates usually require larger impact velocity to splash than droplets on rigid substrates [22].

Given the variation in shapes and sizes among real plants, researchers often employ simplified models, substituting biological specimens with flexible plates or cantilevered beams. These models allow for controlled experimentation and detailed analysis of the interactions between raindrops and plantlike structures. Different orientations of these slender bodies are examined to represent various angles of impact. In horizontal cantilevered setups such as slender plates [23–27] and fibers [28], droplets exhibit diverse responses—being captured [29], ejected [30], or bounced [31]—depending on liquid inertia, capillarity, surface wettability, and cantilever rigidity. These setups are also utilized in droplet-based electricity generators employing triboelectric and piezoelectric techniques [32–35]. Similarly, inclined configurations, where cantilevered fibers are set at specific angles, offer another dimension to study droplet behavior. Studies have proven that such inclination can enhance droplet capturing efficiency [36–39], and by subjecting the fiber to vibration at one end, droplet behavior can be manipulated [40].

In studies focusing on droplet capturing, researchers often employ fibers with fixed ends, thereby neglecting the effects of fiber flexibility [41–44]. These investigations primarily focus on identifying the critical impacting velocities and droplet

*Contact author: zjudengjian@zju.edu.cn

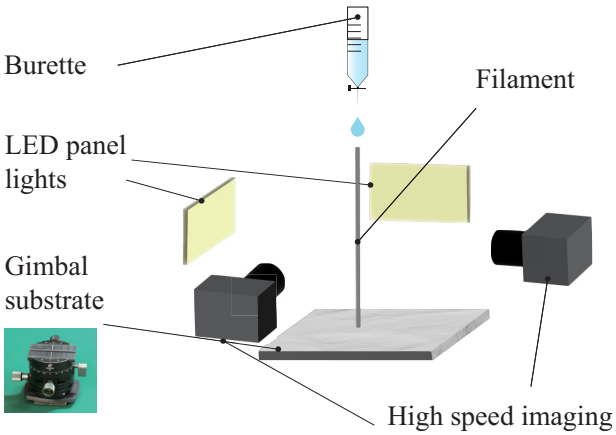

FIG. 1. Conceptual sketch of the experimental setup: Two high-speed cameras are arranged at 90° angles to each other, and two LED light sources are positioned to backlight the filament, facing towards the cameras.

diameters for successful capture [45]. Additionally, droplets impacting needle fibers with noncircular cross sections can spread into various shapes, depending on whether the fiber has a round or wedge profile [46]. Furthermore, droplets dangling down a fiber tend to exhibit two main patterns—barrel and clam-shell shapes—largely determined by droplet size [47].

Here, we present an investigation into the detachment of droplets from an elastic filament clamped at one end and free at the other, initially oriented vertically. Upon axial impact of a falling droplet on the free end, the filament undergoes a dynamic buckling process, as previously documented [48]. It has been observed that the filament exhibits various buckling modes followed by a mode coarsening process, influenced by both the impacting velocity and filament stiffness. However, the post-buckling behavior, particularly whether the droplet will adhere to or detach from the filament, remains unexplored.

To redirect our attention from the initiation of dynamic buckling to the occurrence of droplet detachment, we extend the parameter range utilized in our previous study [48]. Specifically, we elevate the falling height, thereby augmenting the inertia necessary for droplet separation, and elongate the length of the filament to reduce stiffness, encouraging more substantial filament bending and facilitating droplet detachment.

II. METHODS

A. Experiments

Experiments are undertaken to identify the critical conditions required for droplet detachment from a filament, as illustrated in Fig. 1. The intricate dynamics of the droplets and the deflections of the filaments are meticulously captured using two high-speed cameras arranged at 90° angles to each other (2560 × 1600 pixels, 800 fps, Phantom VEO E-340L), facilitating the visualization of three-dimensional deformations. Illumination is provided by two high-intensity LED light sources positioned to backlight the frame, ensuring clear visibility of the filament and droplet interactions.

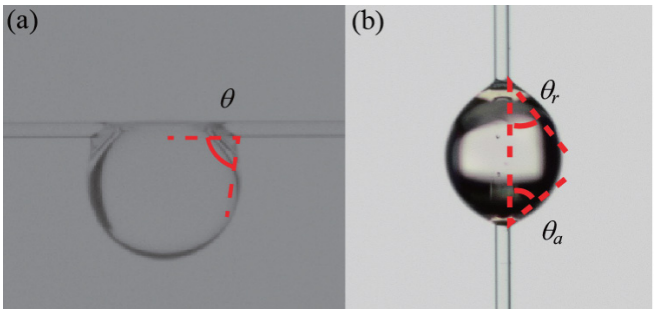

FIG. 2. Experimental images of contact angle measurement. (a) Contact angle θ of a water droplet on a horizontally placed filament in stable equilibrium. (b) Advancing contact angle θ_a and receding contact angle θ_r of the honey droplet on a vertically placed filament.

The filament employed in the experiments has a density of $\rho_f = 2600\ \mathrm{kg/m^3}$ and a circular cross section with a diameter of $d_f = 0.11\ \mathrm{mm}$, possessing a Young's modulus of $E = 75\ \mathrm{GPa}$. A key parameter influencing the stiffness of the filament is its length L, which is varied within the range 7 to 10 cm. The density of the liquid (honey) droplet is $\rho_p = 1410\ \mathrm{kg/m^3}$, with a surface tension of $\sigma = 0.08\ \mathrm{N/m}$ and a dynamic viscosity of $\mu = 950\ \mathrm{Pa\,s}$.

The contact angle and wettability of the filament are carefully measured and are illustrated in Fig. 2. The hydrophilicity of the filament is assessed using the method described by Farhan *et al.* [49], resulting in a contact angle of $80° \pm 3°$ for a water droplet, as shown in Fig. 2(a). The advancing contact angle θ_a and the receding contact angle θ_r of the honey droplet are measured using the approach proposed by Emelyanenko *et al.* [50] as depicted in Fig. 2(b), resulting in $\theta_a = 37° \pm 6°$ and $\theta_r = 28° \pm 5°$. The contact angle hysteresis, defined as the difference between θ_r and θ_a, is thus determined [51]. Therefore, the contact angle of the experimental droplet on the filament falls within the range of $[\theta_r, \theta_a]$.

The droplet falls solely by its own weight through a burette with a needle carefully aligned to guarantee the center of the droplet impacting directly on the top end of the filament. Additionally, a laser leveling instrument is adopted to ensure such alignment. The droplet diameter d_p is varied by using different sizes of burette needles. Since the droplets are driven purely by gravity, those released from the same burette needle maintain nearly identical sizes, which can be easily measured after dripping. The diameters of droplets released from different burette needles are 0.301, 0.316, 0.334, 0.350, 0.367, and 0.386 cm. This range includes values representative of naturally observed raindrops, which typically range from 0.15 to 0.4 cm, as documented in previous studies [52]. The falling heights H span from 7 to 47 cm, corresponding to falling speeds V ranging from 117.1 to 303.5 cm/s. While these speeds are lower than the terminal velocities of typical raindrops, which generally require a descent of approximately 20 m to be reached [52,53], they still provide valuable insights into the dynamics of droplet impacts.

By adjusting the needle size, the falling height, and the filament length, we can systematically study the effects of varying droplet sizes, impact speeds, and structural stiffness

on the detaching process, providing valuable insights into the dynamics of droplet behavior under different conditions.

B. Theoretical model

The linear deformation of the filament can be modeled using the free vibration equation of the Euler-Bernoulli beam with a concentrated mass on the tip, as proposed by Fang *et al.* [27]. Denoting the lateral deformation as $y = y(s,t)$, where s is the coordinate along the beam axis and t represents time, the governing equation for this deformation is given by

$$EI\frac{\partial^4 y(s,t)}{\partial s^4} + \rho_f A\frac{\partial^2 y(s,t)}{\partial t^2} = 0, \tag{1}$$

where I is the moment of inertia (for circular section, $I = \pi d_f^4/64$) and A is the cross-sectional area. The general solution can be written as

$$y(s,t) = \phi(s)A_0\sin(\omega t + \theta_0), \tag{2}$$

where A_0 refers to the amplitude of vibration, written as $A_0 = \pi^2\rho d_p V^2 L^3/3EI$ [31]. θ_0 is the initial phase difference, expressed as $\theta_0 = -\arcsin(\pi\rho g d_p^3 L^3/18EIA)$ [27]. $\phi(s)$ is the mode shape, which can be written as

$$\phi(s) = C_1\cosh\psi s + C_2\sinh\psi s + C_3\cos\psi s + C_4\sin\psi s, \tag{3}$$

where C_1 to C_4 are parameters determined by applying the boundary conditions at the ends of the beam. For the cantilevered configuration, the boundary conditions at the clamped end are $\phi(0) = 0$ and $\phi'(0) = 0$. The initial disturbance is caused by the inertial force of the droplet at the free end of the filament, resulting in $\phi''(L) = 0$ and $EI\phi'''(L) = -M\omega^2\phi(L)$, where $M = \pi\rho_p d_p^3/6$ is the mass of the droplet, and $\omega = \psi^2\sqrt{EI/\rho A}$ is the angular velocity. Therefore, the latent equation can be given as

$$\cos\psi_0\cosh\psi_0 + 1 = \kappa(\sin\psi_0\cosh\psi_0 - \cos\psi_0\sinh\psi_0), \tag{4}$$

where $\kappa = \pi\psi d_p^3/(6AL^2)$, and $\psi_0 = \psi/L$. By solving the above transcendental equation, the only unknown value ψ can be calculated, and accordingly, the mode shape can be obtained.

C. Numerical model

The motion of a flexible filament is modeled using the following equation in a Lagrange form:

$$\rho_f A\frac{\partial^2 \boldsymbol{X}}{\partial t^2} = \frac{\partial}{\partial s}\left(T\frac{\partial \boldsymbol{X}}{\partial s}\right) - \frac{\partial^2}{\partial s^2}\left(\gamma\frac{\partial^2 \boldsymbol{X}}{\partial s^2}\right) + \boldsymbol{F}_\zeta, \tag{5}$$

where $\boldsymbol{X} = [X(s,t), Y(s,t)]$ represents the instantaneous position. The term T denotes the tension force along the filament axis, while $\gamma = EI$ is the bending rigidity of the filament. The damping force $\boldsymbol{F}_\zeta$ is defined as

$$\boldsymbol{F}_\zeta = C_\zeta\frac{\partial \boldsymbol{X}}{\partial t}, \tag{6}$$

where C_ζ is the damping coefficient, set as $C_\zeta \sim O(10^{-5})$ in our cases. The damping force models the dissipative forces acting against the motion of the filament, varying with the velocity. This setup allows for effective simulation of the force relaxation process following droplet impact, capturing the gradual dissipation of kinetic energy as the filament slows down and returns to equilibrium. The tension T is calculated by

$$T = k_s\left(\left|\frac{\partial \boldsymbol{X}}{\partial s}\right| - 1\right), \tag{7}$$

as suggested by the previous study [55], where k_s is the stretching coefficient, set to a very high value [$k_s \sim O(10^2)$], significantly larger than γ [$\gamma \sim O(10^{-7})$] to ensure that the filament remains inextensible under applied forces. This approach effectively prevents any stretching of the filament, allowing it to maintain its length.

The boundary conditions are applied as follows [56]: at the free end,

$$T = 0, \tag{8}$$

$$\frac{\partial^2 \boldsymbol{X}}{\partial s^2} = \boldsymbol{0}, \tag{9}$$

$$\frac{\partial^3 \boldsymbol{X}}{\partial s^3} = \boldsymbol{0}, \tag{10}$$

and at the fixed or clamped end,

$$\frac{\partial \boldsymbol{X}}{\partial s} = \begin{bmatrix}-1\\0\end{bmatrix}. \tag{11}$$

The finite difference method is employed to conduct the simulation. Equation (5) is discretized using a second-order central difference scheme for both spatial and temporal variables. At the tip of the filament, a backward difference scheme is applied, while a forward difference scheme is utilized at the fixed tail. The initial perturbation is given by the impact force obtained from experiments. The duration of this perturbation is determined from the initial moment $t_0 = 0$, when the droplet first contacts the tip of the filament, to the moment t_1, when the velocity of the droplet decreases to 0. During this interval, the droplet transfers its momentum to the filament, causing it to bend. This duration captures the entire interaction between the droplet and the filament, including the initial impact, the subsequent deceleration of the droplet, and the resulting deformation of the filament.

III. RESULTS AND DISCUSSION

A. Mode shapes

The temporal dynamics of droplets impacting the filament are shown in Fig. 3 for some representative cases. The selected time instants are chosen to clearly exhibit the morphology of the filament following droplet impact. Droplets with the same diameter $d_p = 0.386$ cm, falling from a fixed height of $H = 15$ cm, and impacting filaments with lengths $L = 7$, 8, and 9 cm in Figs. 3(a), 3(c) and 3(d), respectively, initially adhere to the filament's tip upon contact. Depending on the filament length, the droplet may either remain on the filament [see Fig. 3(a)] or detach from it [see Figs. 3(c) and 3(d)]. For a filament length of $L = 8$ cm [see Fig. 3(c)], the droplet slides along the tip of the filament over a short distance

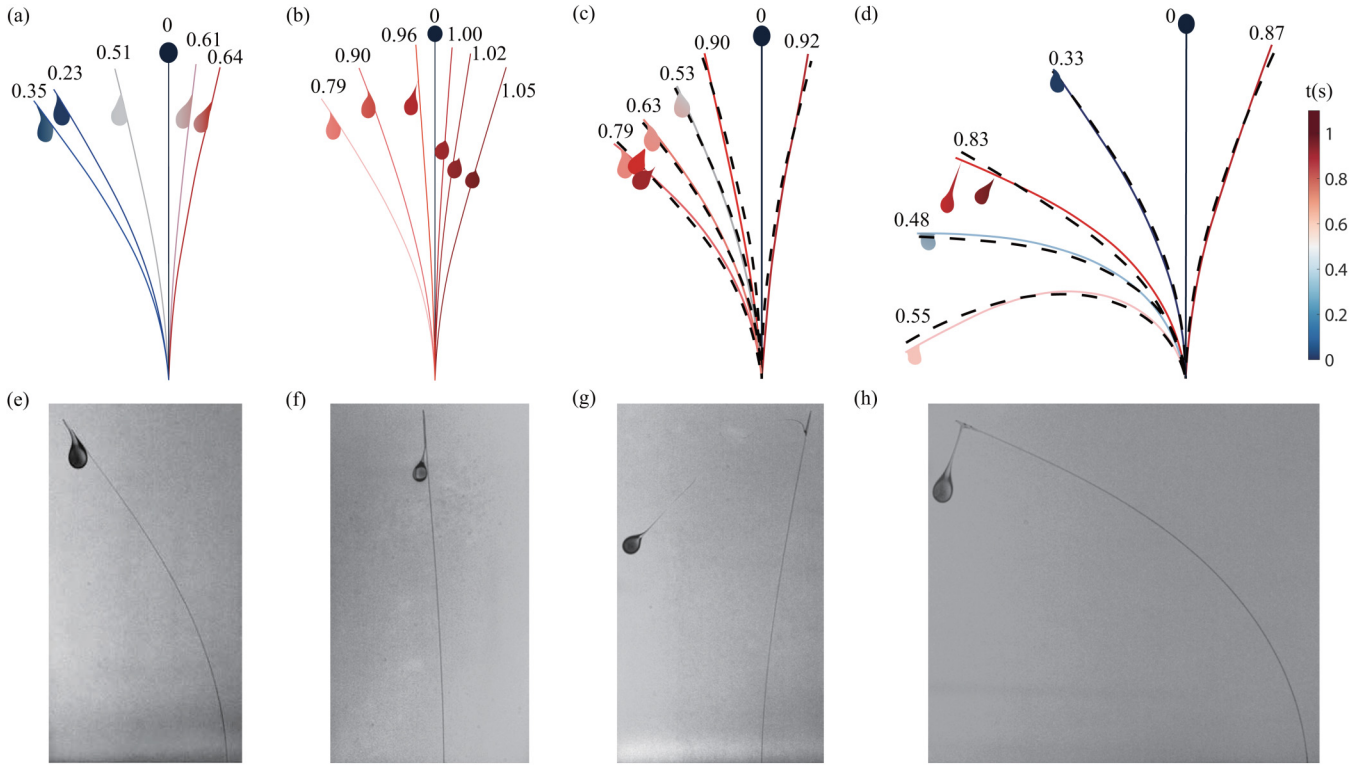

FIG. 3. Temporal dynamics of a droplet impacting a filament: (a) $d_p = 0.386\,\text{cm}$, $H = 15\,\text{cm}$, and $L = 7\,\text{cm}$; (b) $d_p = 0.350\,\text{cm}$, $H = 43\,\text{cm}$, and $L = 8\,\text{cm}$; (c) $d_p = 0.386\,\text{cm}$, $H = 15$, and $L = 8\,\text{cm}$; and (d) $d_p = 0.386\,\text{cm}$, $H = 15$, and $L = 9\,\text{cm}$. The gradient colors represent droplets at different times t in seconds, which are also marked around the filament tips. Solid lines represent experimental results for bending filaments, while dashed lines depict simulation results. Snapshots for the raw experimental images, corresponding to different instants of (e) $t = 0.35\,\text{s}$ in case (a), (f) $t = 0.96\,\text{s}$ in case (b), (g) $t = 0.92\,\text{s}$ in case (c), and (h) $t = 0.83\,\text{s}$ in case (d). Supplemental Movies S1 to S4 in Ref. [54] correspond to the experimental observations.

before reaching the maximum bending state. In contrast, for a filament length of $L = 9\,\text{cm}$ [see Fig. 3(d)], the droplet remains relatively stationary on the surface with minimal movement. When the filament reaches its maximum bending extent [see Fig. 3(c) at $t = 0.79\,\text{s}$ and Fig. 3(d) at $t = 0.55\,\text{s}$], it reverses its bending direction. During this reversal, a liquid bridge forms between the droplet crest and the filament [see Fig. 3(d) at $t = 0.83\,\text{s}$]. Subsequently, the liquid film ruptures as the filament moves further, leading to droplet detachment.

An interesting observation is the recapture event shown in Fig. 3(b), where the droplet initially detaches from the filament [see Fig. 3(b) at $t = 0.96\,\text{s}$] and then falls back onto it and is recaptured [see Fig. 3(b) at $t = 1\,\text{s}$]. This phenomenon occurs in cases with small droplet diameters near the critical falling height, such as $d_p = 0.350\,\text{cm}$ and $H = 43\,\text{cm}$, as illustrated in the phase-space diagram in Fig. 5. It is noteworthy that the filament deformations obtained from time-dependent numerical simulations, represented by dashed lines in Fig. 3, closely match the experimental observations.

The theoretical solutions for the tip displacement over time are illustrated in Fig. 4(a). In this analysis, we consider cases with $d_p = 0.316\,\text{cm}$ and $H = 31\,\text{cm}$, while varying the lengths of the filaments. All filaments exhibit linear deformation. Notably, as the filament length L increases, the maximum tip displacement also increases, and it takes longer to reach that position. This behavior is intuitive, as a longer filament implies lower stiffness, resulting in comparatively larger deformation under the same impact force.

For further analysis, we introduce the bending angle, denoted as θ_b, which measures the angle between the filament's initial straight state and the position where the tip reaches its maximum deflection. A critical value of $\theta_{bc} = 65^\circ$ is identified experimentally and plotted as a green dashed line in Fig. 4(b), distinguishing between two distinct bending modes. For bending angles less than this critical value, we observe the first bending mode, depicted in Fig. 3(c). In this mode, the filament exhibits single curvature throughout the bending process. However, for θ_b greater than θ_{bc}, we observe the second bending mode, demonstrated in Fig. 3(d), where the filament displays double curvature upon bending beyond θ_{bc}, or when the tip reaches below the crest of the filament.

For filaments with $L = 7$, 8, and 9 cm, the influence of the falling height H of the impacting droplet is conspicuous, with the bending angle becoming larger as H increases. The dependence on the monotonic increase of the falling height reflects that the inertia of the droplet greatly affects the bending angle within this range of filament lengths. For $L = 9\,\text{cm}$, a notable transition occurs in the bending mode: at a critical falling height of $H = 15\,\text{cm}$, the filament shifts from the first bending mode to the second bending mode. During the first bending mode regime, there is a pronounced increase in the bending angle with increasing H. Beyond this point, the effect of H diminishes but still exists, indicating that the

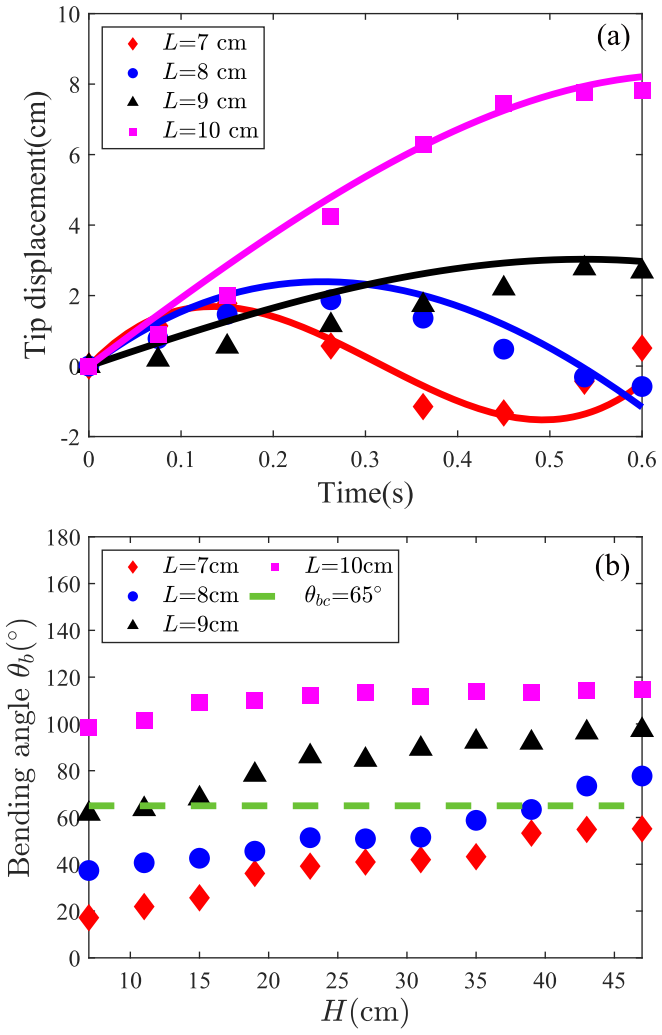

FIG. 4. (a) Tip displacement over time for different filament lengths L, with symbols representing experimental data and solid lines representing theoretical results obtained from Eq. (1). The diameter of the droplet is $d_p = 0.316$ cm, and the falling height is $H = 31$ cm. (b) Bending angles of filaments with lengths of $L = 7$, 8, 9, and 10 cm, impacted by the droplet of $d_p = 0.386$ cm for the height of $H = 7$–47 cm. The dashed line represents the critical bending angle that equals 65°.

effect of inertia plays a more significant role within the first bending mode range and gradually decreases in the second bending mode range. Similarly, for filaments with $L = 10$ cm, variations in the falling height have minimal impact on the bending angle since the filaments exhibit only the second bending mode throughout this range of H. This observation underscores that the influence of inertia is more pronounced in the first bending mode and lessens as the filament transfers to the second bending mode. The main reason is that in the second bending mode regime, the filaments are more likely to buckle under static loads rather than dynamic loads. This has been further validated through subsequent energy analysis.

B. Detachment on H-d_p parameter space

The motion of the droplet is governed by various forces acting upon it. It is primarily driven downwards by the gravitational force F_g, and it encounters resistance from multiple sources, including form drag force F_d, viscous force F_v, and capillary force F_s. We define the Weber number as $\mathrm{We} = \rho_p V^2 d_p/\sigma$. In our experimental setup, we identify Weber numbers ranging from 72 to 626. This broad range suggests that the influence of capillary force is minimal, allowing us to disregard it in our analysis [36]. This simplification enables a clearer focus on the dominant forces shaping the behavior of the droplet.

We apply a momentum-conservation model to delineate attached and detached regimes in the H-d_p parametric space. Upon impact, the impulse causes momentum transfer, expressed as

$$M\Delta V = (-F_d - F_v + F_g)\Delta t, \tag{12}$$

where $\Delta V = V_f - V$ represents the change in falling speed after detachment. It is important to note that the range of momentum changes considered in this analysis spans from the instant $t_0 = 0$, when the droplet contacts the filament to t_1, when the velocity of the droplet reaches 0. This period encompasses the initial impact and the subsequent deceleration phase, capturing the primary interaction between the droplet and the filament. Any post-impact motion of the droplet, such as sliding along the filament, falls outside the scope of this analysis. The exclusion of the post-impact behavior of the droplet focuses the analysis on the immediate effects of the impact, ensuring a clear understanding of the initial momentum transfer and its influence on the bending dynamics of the filament. Therefore, V signifies the impact speed ($V \simeq \sqrt{2gH}$ [43]) just before contact, and V_f represents the moment when the droplet stops moving and is set as 0 [41]. The duration Δt is equal to the detachment time t_d observed from the experiments.

The forces can be expressed explicitly as follows: the form drag force $F_d \sim (1/2)\rho_p V^2 d_p d_f$ [45]; the viscous force $F_v \sim (1/2)\pi\mu d_f V\sqrt{\lambda_\sigma/d_f}$, where $\lambda_\sigma = \sqrt{\sigma/(\rho_p g)}$ represents the capillary length [57]; and the gravitational force $F_g \sim Mg$, with $g = 9.8$ m^2/s. Substituting the above expressions into Eq. (12), we obtain a critical falling height H_{c1} that determines the detachment of the droplet:

$$H_{c1} = \left[\frac{M - \sqrt{M^2 - 2\zeta t_d^2(F_v - F_g)}}{\sqrt{2g}\rho_p d_p d_f t_d}\right]^2, \tag{13}$$

This formula defines the transition between attached and detached droplets, as a function of the different parameters, including d_p, as illustrated by the dashed line in Fig. 5. The transition boundary, obtained using the momentum-conservation model, closely aligns with the experimental data. For a given filament length, there exists a threshold impact speed varying with the droplet size, or equivalently the critical falling height, which decreases nonlinearly with the growth of droplet size. Smaller droplets require a significantly higher falling height to impart sufficient kinetic energy for detachment, while larger droplets have a comparatively lower critical height.

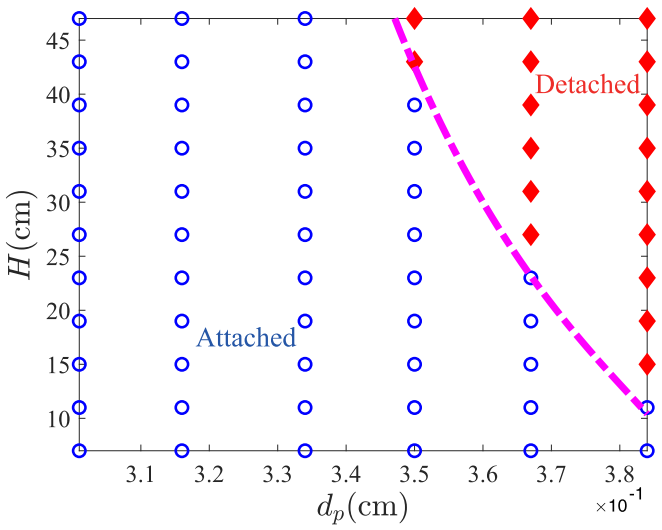

FIG. 5. Detaching regime in the parameter space of the falling height H and the droplet diameter d_p, at a fixed filament length of $L = 8$ cm. The symbols represent experimental data, with the red solid diamonds denoting detachment cases and the hollow blue circles denoting adhering droplets. The transition between the two as predicted by Eq. (13) is indicated by the dashed line.

C. Detachment on H-L parameter space

Exploring how the kinetic energy of a falling droplet transforms into the elastic energy of the filament provides valuable insights into the detachment phenomenon. To investigate this relationship, we keep the droplet diameter constant and analyze the results in the H-L parameter space.

For a deformed filament, its elastic bending energy can be calculated for large deformations as [58]

$$E_b = \frac{1}{2}EI\int_0^L \left[\frac{y''}{(1+y'^2)^{3/2}}\right]^2 dx, \tag{14}$$

where y is determined from experimental snapshots, and x denotes the filament axis. At any given time, the bending energy can be calculated using Eq. (14), with the maximum bending energy $E_{b,\max}$ occurring at the maximum bending state [see Fig. 3(c) at $t = 0.79$ s, and 3(d) at $t = 0.55$ s].

We choose a specific droplet with a diameter of $d_p = 0.386$ cm to examine how much kinetic energy can be converted into elastic energy of the filament after impact. We draw a contour map of the maximum bending energy $E_{b,\max}$ in the H-L parameter space using experimental data, as shown in Fig. 6. As expected, the maximum bending energy gets higher as we increase either the filament length or the droplet falling height. In Fig. 6, the green dots represent the boundary between the adhered and detached regimes, obtained from our experimental observation. To rationalize this transition boundary, we attempt to develop a theoretical framework. The kinetic energy of the droplet as it reaches the filament tip is denoted as $E_k = (1/2)MV^2$ or $\sim MgH$ by neglecting the air resistance as the droplet falls. We assume that the impact force takes the form of inertia $F_I \sim (1/2)\rho_p V^2 d_p d_f$, which is reasonable since the Reynolds number ($\mathrm{Re} = \rho_p V d_p/\mu$) is in the range of 5.2–17.3, suggesting that inertial force dominates over viscous force. The bending force can be approximated as

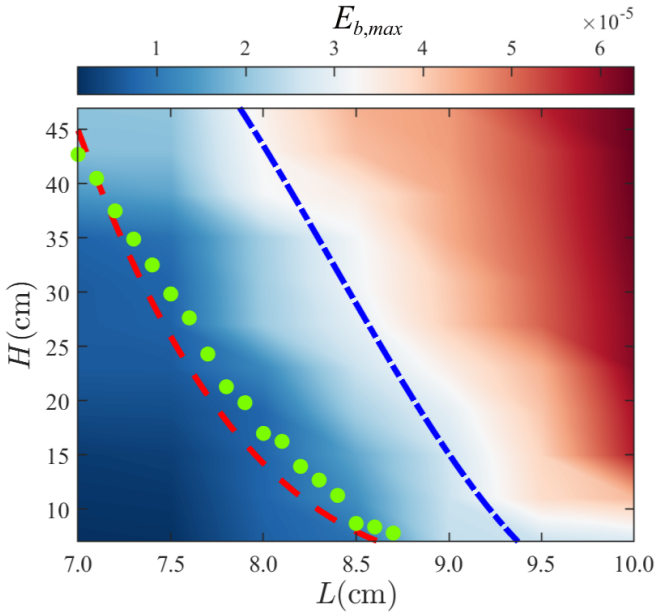

FIG. 6. Contours depicting the maximum bending energy $E_{b,\max}$ in the H-L parameter space for a fixed droplet diameter of $d_p = 0.386$ cm. The contours are plotted on a mesh with intervals $\Delta H = 4$ cm and $\Delta L = 0.5$ cm. The red dashed line, determined by Eq. (18), delineates the boundary between detached (upper right) and attached (lower left) regions. Experimental data points (green dots) are included, with filament length intervals of $\Delta L = 0.1$ cm. The blue dash-dotted line, derived from experiments, indicates the transition between the first and second bending modes.

$F_B \sim EI/L^2$. Therefore, the force ratio can be expressed as a Cauchy number:

$$\mathrm{Ca} = \frac{\rho_p V^2 d_p d_f L^2}{2EI} = \beta H L^2, \tag{15}$$

where the coefficient β is a constant depending on the properties of the droplet and filament,

$$\beta = \frac{\rho_p g d_p d_f}{EI}. \tag{16}$$

For each filament length, we experimentally identify a critical velocity of impact, or a critical falling height (represented by the green dots in Fig. 6), through which we can define a critical Cauchy number Ca_c. The energy conversion rate is defined as $r_1 = E_{b,\max}/E_k$, which is obtained from experimental data. Surprisingly, we find that the relationship between r_1 and Ca_c^{-1} can be linearly fitted, with a slope of 0.9π, as shown in Fig. 7(a), so that we can write

$$r_1 = 0.9\pi \mathrm{Ca}_c^{-1} = \frac{0.9\pi}{\beta H_{c2} L^2}. \tag{17}$$

Consequently, the critical falling height H_{c2} can be expressed as a function of the filament length L,

$$H_{c2} = \frac{0.9\pi}{\beta r_1}\frac{1}{L^2}. \tag{18}$$

This critical boundary is shown in Fig. 6 by a red dashed line, separating the detached and attached scenarios. Cases to the left of this line remain attached, while those to the right result in detachment. It can be seen that the boundary fits well with

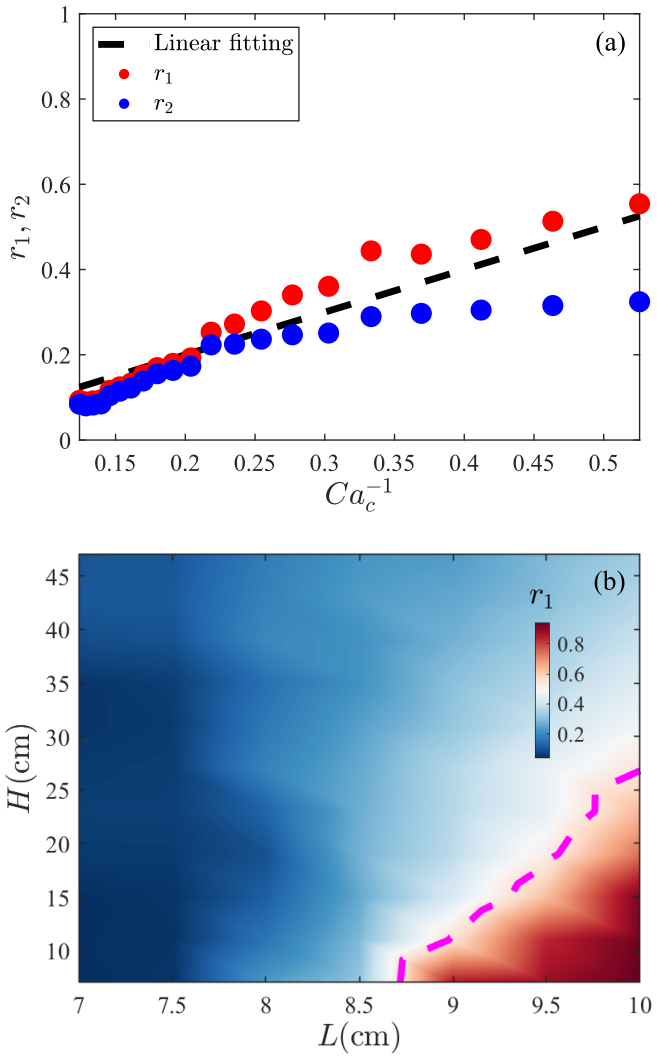

FIG. 7. (a) Variation of the kinetic energy conversion rate $r_1 = E_{b,\max}/E_k$ and the total energy conversion rate $r_2 = E_{b,\max}/E_{\text{tot}}$ with coefficient Ca_c^{-1}. The dots represent experimental data, and the dashed line is the linear fitting. (b) Contours of r_1 on the H-L parameter space for a droplet diameter $d_p = 0.386$ cm, with a dashed-line marking the maximum Ca_c^{-1} in panel (a), which is 0.53.

the experimental data (green dots). The blue dash-dotted line, derived from experimental observations, separates the two bending modes: to the left is the first bending mode, as noticed in Fig. 3(c), and to the right is the second bending mode, as seen in Fig. 3(d). It becomes evident that, if the filament undergoes the second bending mode, then the detachment of the droplet is bound to occur. However, the droplet is not guaranteed to stay attached if the filament undergoes the first bending mode. Theoretically, for a filament exhibiting the first bending mode, the length L and the maximum bending energy $E_{b,\max}$ are comparatively small, causing the critical impact height to be large according to Eq. (18). In other words, the threshold for the droplet to detach is lower than that for the filament to reach the second bending mode but higher than that for it to reach the first bending mode. Therefore, the bending mode cannot be treated as the sole criterion for the droplet detachment. The convincing proof is Eq. (18), which accounts for the interplay between filament length, bending energy, and impact height, providing a more comprehensive understanding of the conditions leading to droplet detachment.

It is worthy further discussing the energy conversion. As shown in Fig. 7(a), the maximum value of r_1 is obtained at $\text{Ca}_c^{-1} = 0.53$, corresponding to the bottom right green dot at $L = 8.7$ cm, in Fig. 6. Beyond this critical value of Ca_c^{-1}, r_1 keeps increasing. Note that in this case the additional potential energy associated with the descent of the droplet along the filament cannot be ignored. We therefore also plot the ratio $r_2 = E_{b,\max}/E_{\text{tot}}$ between the maximum bending energy and the sum of the impacting kinetic energy and the gravity potential energy after this impact, or equivalently the total potential energy from the release point to the maximum bending position, as seen in Fig. 7(b). The data show that r_2 stops rising as we further increase Ca_c^{-1}. It is important to note that in the lower-right corner in the H-L parameter space, where the droplet contacts the filament at a low speed, the filament buckles more akin to a static load being imposed on the tip of the filament. This differs from the "dynamic impact" scenario we are currently addressing. In the dynamic buckling regime, i.e., the left part of Fig. 7(b), the filament's dynamic buckling and the subsequent mode-coarsening process during the post-buckling stage dissipate mechanical energy more effectively, resulting in lower-energy conversion rates.

IV. CONCLUSION

In summary, we study the detachment of droplets from vertically oriented elastic filaments, exploring the influence of three key control parameters: the length of the filament, L; the falling height of the droplet, H; and the diameter of the droplet, d_p. The falling height and the droplet size determine the magnitude of the impact force during contact.

Experimental observations reveal two distinct bending modes, distinguished by a critical bending angle θ_{bc}. The first bending mode, associated with smaller deformations, is analyzed using the Euler-Bernoulli beam equation, which accurately models the linear elastic behavior of the filament. The second bending mode, associated with nonlinear large deformations, has been analyzed using time-dependent numerical simulations to capture the complex dynamics involved. Both theoretical and numerical approaches corroborate the experimental findings, providing a comprehensive understanding of the filament's response to droplet impact.

Two regimes are established in the H-d_p and H-L parameter spaces to differentiate between attached and detached droplets. Momentum-conservation and energy conversion models are employed to determine critical falling heights in each regime, showing good agreement with experimental data. Furthermore, a dimensionless Cauchy number, derived from the ratio of inertial force to bending force, correlates linearly with the ratio of the maximum bending energy to the kinetic energy of the droplet, setting the transition boundary between inertia- and gravity-dominated detachment situations.

This investigation enhances our fundamental understanding of the factors influencing the detaching behavior of a droplet upon impacting a flexible filament. The framework derived from this study holds potential applicability in various biological systems, and the energy conversion rate provides in-depth insights for the development of droplet-based

electricity generators. Future research endeavors could explore the internal fluid dynamics within the droplet and delve into the mechanisms governing film rupture and coalescence on the filament.

ACKNOWLEDGMENT

This research has been supported by the National Natural Science Foundation of China (Grant No. 92252102).

[1] A. Roth-Nebelsick, W. Konrad, M. Ebner, T. Miranda, S. Thielen, and J. H. Nebelsick, When rain collides with plants—patterns and forces of drop impact and how leaves respond to them, J. Exp. Bot. **73**, 1155 (2022).

[2] S. Kim, H. Park, H. A. Gruszewski, D. G. Schmale, III, and S. Jung, Vortex-induced dispersal of a plant pathogen by raindrop impact, Proc. Natl. Acad. Sci. USA **116**, 4917 (2019).

[3] A.-K. Lenz, U. Bauer, and G. D. Ruxton, An ecological perspective on water shedding from leaves, J. Exp. Bot. **73**, 1176 (2022).

[4] L. K. Lauderbaugh and C. D. Holder, The biomechanics of leaf oscillations during rainfall events, J. Exp. Bot. **73**, 1139 (2022).

[5] S. Kim, Z. Wu, E. Esmaili, J. J. Dombroskie, and S. Jung, How a raindrop gets shattered on biological surfaces, Proc. Natl. Acad. Sci. USA **117**, 13901 (2020).

[6] A. K. Dickerson, Z. G. Mills, and D. L. Hu, Wet mammals shake at tuned frequencies to dry, J. R. Soc., Interface **9**, 3208 (2012).

[7] Q. Meng, Q. Wang, H. Liu, and L. Jiang, A bio-inspired flexible fiber array with an open radial geometry for highly efficient liquid transfer, NPG Asia Mater. **6**, e125 (2014).

[8] Q. Wang, X. Yao, H. Liu, D. Quéré, and L. Jiang, Self-removal of condensed water on the legs of water striders, Proc. Natl. Acad. Sci. USA **112**, 9247 (2015).

[9] X. Wang, W. Zhang, S. Li, Z. Guo, and W. Liu, An efficient fog collector inspired by Tillandsia and cactus spines, Chem. Eng. J. **472**, 145042 (2023).

[10] H. Venkatesan, J. Chen, H. Liu, W. Liu, and J. Hu, A spider-capture-silk-like fiber with extremely high-volume directional water collection, Adv. Funct. Mater. **30**, 2002437 (2020).

[11] S. Chen, F. Yang, and Z. Guo, Transport and collection of water droplets interacting with bioinspired fibers, Adv. Colloid Interface Sci. **309**, 102779 (2022).

[12] Y. Hou, Y. Chen, Y. Xue, Y. Zheng, and L. Jiang, Water collection behavior and hanging ability of bioinspired fiber, Langmuir **28**, 4737 (2012).

[13] D. Zhan and Z. Guo, Overview of the design of bionic fine hierarchical structures for fog collection, Mater. Horiz. **10**, 4827 (2023).

[14] Y. Liu, X. Peng, L. Zhu, R. Jiang, J. Liu, and C. Chen, Liquid-assisted bionic conical needle for in-air and in-oil–water droplet ultrafast unidirectional transportation and efficient fog harvesting, ACS Appl. Mater. Interfaces **15**, 59920 (2023).

[15] D. Gurera and B. Bhushan, Optimization of bioinspired conical surfaces for water collection from fog, J. Colloid Interface Sci. **551**, 26 (2019).

[16] C. Josserand and S. T. Thoroddsen, Drop impact on a solid surface, Annu. Rev. Fluid Mech. **48**, 365 (2016).

[17] L. Gordillo, T.-P. Sun, and X. Cheng, Dynamics of drop impact on solid surfaces: Evolution of impact force and self-similar spreading, J. Fluid Mech. **840**, 190 (2018).

[18] B. Zhang, J. Li, P. Guo, and Q. Lv, Experimental studies on the effect of Reynolds and Weber numbers on the impact forces of low-speed droplets colliding with a solid surface, Exp. Fluids **58**, 125 (2017).

[19] J. C. Bird, R. Dhiman, H.-M. Kwon, and K. K. Varanasi, Reducing the contact time of a bouncing drop, Nature (London) **503**, 385 (2013).

[20] J.-H. Kim, J. P. Rothstein, and J. K. Shang, Dynamics of a flexible superhydrophobic surface during a drop impact, Phys. Fluids **30**, 072102 (2018).

[21] Q. Vo and T. Tran, Critical conditions for jumping droplets, Phys. Rev. Lett. **123**, 024502 (2019).

[22] C. J. Howland, A. Antkowiak, J. R. Castrejón-Pita, S. D. Howison, J. M. Oliver, R. W. Style, and A. A. Castrejón-Pita, It's harder to splash on soft solids, Phys. Rev. Lett. **117**, 184502 (2016).

[23] S. Gart, J. E. Mates, C. M. Megaridis, and S. Jung, Droplet impacting a cantilever: A leaf-raindrop system, Phys. Rev. Appl. **3**, 044019 (2015).

[24] X. Huang, X. Dong, J. Li, and J. Liu, Droplet impact induced large deflection of a cantilever, Phys. Fluids **31**, 062106 (2019).

[25] P. Orkweha, A. Downing, A. P. Lebanoff, S. Zehtabian, S. S. Bacanli, D. Turgut, and A. K. Dickerson, Ensemble machine learning predicts displacement of cantilevered fibers impacted by falling drops, J. Fluids Struct. **102**, 103253 (2021).

[26] S. Lee, S. Joung, and D. Kim, Dynamics of a droplet-impact-driven cantilever making contact with the ground, Phys. Fluids **34**, 042125 (2022).

[27] W. Fang, S. Wang, H. Duan, S. A. Tahir, K. Zhang, L. Wang, X.-Q. Feng, and M. Song, Target slinging of droplets with a flexible cantilever, Droplet **2**, e72 (2023).

[28] E. Dressaire, A. Sauret, F. Boulogne, and H. A. Stone, Drop impact on a flexible fiber, Soft Matter **12**, 200 (2016).

[29] J. Comtet, B. Keshavarz, and J. W. Bush, Drop impact and capture on a thin flexible fiber, Soft Matter **12**, 149 (2016).

[30] M. E. Alam, J. L. Kauffman, and A. K. Dickerson, Drop ejection from vibrating damped, dampened wings, Soft Matter **16**, 1931 (2020).

[31] G. Upadhyay, V. Kumar, and R. Bhardwaj, Bouncing droplets on an elastic, superhydrophobic cantilever beam, Phys. Fluids **33**, 042104 (2021).

[32] G. Hao, X. Dong, and Z. Li, A novel piezoelectric structure for harvesting energy from water droplet: Theoretical and experimental studies, Energy **232**, 121071 (2021).

[33] L. Wang, W. Li, Y. Song, W. Xu, Y. Jin, C. Zhang, and Z. Wang, Monolithic integrated flexible yet robust droplet-based electricity generator, Adv. Funct. Mater. **32**, 2206705 (2022).

[34] M. Zhang, C. Bao, C. Hu, Y. Huang, Y. Yang, and Y. Su, A droplet-based triboelectric-piezoelectric hybridized nanogenerator for scavenging mechanical energy, Nano Energy **104**, 107992 (2022).

[35] X. Xu, Y. Wang, P. Li, W. Xu, L. Wei, Z. Wang, and Z. Yang, A leaf-mimic rain energy harvester by liquid-solid contact

electrification and piezoelectricity, Nano Energy **90**, 106573 (2021).
[36] K. Piroird, C. Clanet, É. Lorenceau, and D. Quéré, Drops impacting inclined fibers, J. Colloid Interface Sci. **334**, 70 (2009).
[37] C. Wang, X. Wu, H. Zhang, P. Hao, F. He, and X. Zhang, A many-body dissipative particle dynamics study of eccentric droplets impacting inclined fiber, Phys. Fluids **33**, 042001 (2021).
[38] A. Pour Karimi, M. Rietz, W. Rohlfs, B. Scheid, and R. Kneer, Experimental study of dripping, jetting and drop-off from thin film flows on inclined fibers, Eur. Phys. J.: Spec. Top. **232**, 443 (2023).
[39] M. Amrei, D. Venkateshan, N. D'Souza, J. Atulasimha, and H. V. Tafreshi, Novel approach to measuring the droplet detachment force from fibers, Langmuir **32**, 13333 (2016).
[40] A. Bick, F. Boulogne, A. Sauret, and H. A. Stone, Tunable transport of drops on a vibrating inclined fiber, Appl. Phys. Lett. **107**, 181604 (2015).
[41] S.-G. Kim and W. Kim, Drop impact on a fiber, Phys. Fluids **28**, 042001 (2016).
[42] S. Abishek, R. Mead-Hunter, A. J. C. King, and B. J. Mullins, Capture and re-entrainment of microdroplets on fibers, Phys. Rev. E **100**, 042803 (2019).
[43] P. Zhu, W. Wang, X. Chen, F. Lin, X. Wei, C. Ji, and J. Zou, Experimental study of drop impact on a thin fiber, Phys. Fluids **31**, 107102 (2019).
[44] N. Ojaghlou, H. V. Tafreshi, D. Bratko, and A. Luzar, Dynamical insights into the mechanism of a droplet detachment from a fiber, Soft Matter **14**, 8924 (2018).
[45] É. Lorenceau, C. Clanet, and D. Quéré, Capturing drops with a thin fiber, J. Colloid Interface Sci. **279**, 192 (2004).
[46] A. P. Lebanoff and A. K. Dickerson, Drop impact onto pine needle fibers with non-circular cross section, Phys. Fluids **32**, 092113 (2020).
[47] T.-H. Chou, S.-J. Hong, Y.-E. Liang, H.-K. Tsao, and Y.-J. Sheng, Equilibrium phase diagram of drop-on-fiber: Coexistent states and gravity effect, Langmuir **27**, 3685 (2011).
[48] M. Lu, J. Deng, X. Mao, and L. Brandt, Dynamic buckling of a filament impacted by a falling droplet, Phys. Rev. Lett. **131**, 184002 (2023).
[49] N. M. Farhan, H. Aziz, and H. V. Tafreshi, Simple method for measuring intrinsic contact angle of a fiber with liquids, Exp. Fluids **60**, 87 (2019).
[50] A. Emelyanenko, N. Ermolenko, and L. Boinovich, Contact angle and wetting hysteresis measurements by digital image processing of the drop on a vertical filament, Colloids Surf., A **239**, 25 (2004).
[51] A. Marmur, C. Della Volpe, S. Siboni, A. Amirfazli, and J. W. Drelich, Contact angles and wettability: Towards common and accurate terminology, Surf. Innovations **5**, 3 (2017).
[52] J. O. Laws, Measurements of the fall-velocity of water-drops and raindrops, Eos, Trans. Am. Geophys. Union **22**, 709 (1941).
[53] M. Szakall, S. K. Mitra, K. Diehl, and S. Borrmann, Shapes and oscillations of falling raindrops—a review, Atmos. Res. **97**, 416 (2010).
[54] See Supplemental Material at http://link.aps.org/supplemental/10.1103/PhysRevResearch.6.043003 for the supplemental videos.
[55] J. Deng, X. Mao, and F. Xie, Dynamics of two-dimensional flow around a circular cylinder with flexible filaments attached, Phys. Rev. E **100**, 053107 (2019).
[56] W.-X. Huang, S. J. Shin, and H. J. Sung, Simulation of flexible filaments in a uniform flow by the immersed boundary method, J. Comput. Phys. **226**, 2206 (2007).
[57] T. Gilet, D. Terwagne, and N. Vandewalle, Droplets sliding on fibres, Eur. Phys. J. E **31**, 253 (2010).
[58] S. P. Timoshenko and J. M. Gere, *Theory of Elastic Stability* (Courier, New York, 2012).